# Supporting Online Material for

## How Much More Rain Will Global Warming Bring?

Frank J. Wentz,* Lucrezia Ricciardulli, Kyle Hilburn, Carl Mears

*To whom correspondence should be addressed. E-mail: frank.wentz@remss.com

Published 31 May 2007 on *Science* Express
DOI: 10.1126/science.1140746

**This PDF file includes:**

# Supporting Online Material: Materials and Methods

## 1. Computation of evaporation over the ocean

We compute evaporation over the oceans using the bulk formula from the NCAR Community Atmospheric Model 3.0 (S1). The rate of evaporation is proportional to the vertical gradient of specific humidity at the Earth's surface, which can be expressed by the bulk aerodynamic method:

$$E = \frac{\kappa\sqrt{\rho\tau_0}\,(q_0 - q_z)}{\ln\frac{z}{z_0} - \psi} \tag{S1}$$

where $\kappa$ is von Karman's constant, $\rho$ is the surface air density, $\tau_0$ is surface wind stress, $q_0$ and $q_z$ are the specific humidities at the surface and at height $z$. The terms $z_0$ and $\psi$ are the roughness length and profile for latent heat flux. One advantage of using satellite wind retrievals as opposed to *in situ* wind measurements is that the satellite retrievals are a direct measurement of surface stress. Given $\tau_0$, the bulk formulation simplifies in that the momentum drag coefficient is not needed. The specific humidities $q_0$ and $q_z$ are functions of the sea-surface temperature (SST), the air temperature at height $z$, and the relative humidity (RH) at height $z$. These three terms come from ancillary datasets.

For SST we use the Reynolds' optimum interpolated product (OISST), which is derived from satellite infrared SST retrievals that are calibrated to *in situ* SST observations (S2). The marine air temperature (MAT) dataset comes from the Hadley Center (S3). The MATs are a quality-controlled global dataset of ship and buoy air temperature measurements, averaged over a 5° monthly grid. During the SSM/I period, the reference height for these air temperature measurements is $z$ = 15 m. Only nighttime measurements are used to avoid biases due to solar heating of the ship decks.

We find that from 1987-2006 the MATs are cooling by 0.06 K decade$^{-1}$ relative to the SST. This relative cooling trend in the MAT dataset has been noted elsewhere (S4) and was used to support early results from the satellite microwave sounding unit (MSU). This earlier version of MSU observations indicated the tropical lower troposphere (TLT) was not warming as much as the surface. However, an error in the methodology applied to the MSU was later found (S5), and the new results indicate the TLT is in fact warming faster than the surface as predicted by most climate models.

Given these new MSU results, it is difficult to explain the relative cooling trend in the MAT. Furthermore, if the cooling trend were real, the corresponding reduction in static stability would increase E by an additional 0.6% decade$^{-1}$ to a value near 2% decade$^{-1}$. We do not consider such a large increase in evaporation as plausible. It is not consistent with the precipitation results and it is way out of line with climate model predictions (S6). Therefore, the relative cooling in the MAT is assumed to be a spurious artifact and is not incorporated it into our analysis. Rather, we average the difference $\Delta$T = MAT - SST over 19 years and make climatology maps of $\Delta$T at a 2.5° spatial resolution for each of the 12 months.

For RH we use the International Comprehensive Ocean-Atmosphere Data Set (ICOADS) (S7). We made trend maps of the ICOADS relative humidities and found no appreciable trends

that are above the noise level. This is in agreement with climate models, which in general predict little change in RH with global warming (S6, S8). The assumption of constant RH is also supported by *in situ* observations (S9) and satellite observations (S10). We treat the ICOADS dataset the same as the MAT dataset: we average over the 19 years and make 12 monthly climatology maps of RH.

## 2. Evaporation over land and ice

The estimation of evaporation over land is a difficult problem. Satellite estimates of $\tau_0$ are not available, and other parameters such as soil moisture and land cover come into play. Fortunately for our analysis the contribution of land to global evaporation is only 14%, and we expect the contribution of land to the long-term variability of E to be small, albeit it is a source of error. We use a constant value of 527 mm $yr^{-1}$ for all the continents excluding Antarctic (S11). Any actual trends in land evaporation would be a source of error in our results. For example the Global Precipitation Climatology Project (GPCP) (S12) precipitation values just over land for the 1987-2006 period show an increase of 14 mm $yr^{-1}$ $decade^{-1}$. This might suggest an accompanying increase in evaporation over land due to more available surface water and soil moisture. If we were to assume E=P over land rather than using a static value for E, the global evaporation trend would increase from 1.3 % $decade^{-1}$ to 1.7 % $decade^{-1}$, giving us an even larger discrepancy with the climate model predictions. On the other hand, pan evaporation measurements possibly show a decrease in land evaporation, but the interpretation of these results is far from settled (S13). In any event, trends in the evaporation over land may have a small effect on our results, but it is unlikely that it will be large enough to change the basic conclusions of the study.

For Antarctica and sea ice we use a value of 28 mm $yr^{-1}$ (S11). SSM/I measures the varying extent of the sea ice, and our method does accounts for the decline in the arctic sea ice. However the effect of declining sea ice on global evaporation is very small, being about +0.02% $decade^{-1}$.

# Supporting Online Material: Text

## 1. SSM/I background

The Special Sensor Microwave Imager (SSM/I) is provided by the U.S. Defense Meteorological Satellite Program (DMSP). DMSP typically maintains two to three polar orbiting satellites in operation at any give time. The DMSP F08 satellite, which was launched in June 1987, flew the first SSM/I, and since then, five additional SSM/Is have been launched, with the last three still in operation as of the end of 2006. The SSM/I views the Earth in the spectral region from 19 to 85 GHz. The spectral and polarimetric information in this band is sufficient to retrieve a number of important geophysical parameters. Particularly accurate retrievals can be done over the world's oceans because a water surface provides a radiometrically cold background with a precisely known spectral and polarimetric signature. The over-ocean SSM/I retrievals include: surface wind stress, total atmospheric water vapor and cloud water, surface rain rate, and sea-ice extent (S14).

Realizing the potential importance of SSM/I observations to climate research, Remote Sensing Systems (RSS) early on initiated rigorous quality control procedures and advanced sensor calibration techniques to convert the SSM/I operational weather products into research-quality climate products (S15). Much of the early evidence of the decline in the Arctic sea ice extent came from analyses of these SSM/I observations (S16). Another important SSM/I finding was the close coupling between tropospheric warming and moistening (S10). This was revealed by comparing the decadal timeseries of SSM/I water vapor with the lower tropospheric temperatures coming from another series of satellite sensors: the microwave sounding unit (MSU).

The methods for retrieving precipitation (P), water vapor (V), and surface stress ($\tau_0$) from the SSM/I microwave radiances are quite different. Precipitation retrievals are based on observing a spectral signature in the radiances that increases with frequency. The water vapor retrieval relies on the 22-GHz channel, which is centered on a weak water vapor absorption line. The retrieval of $\tau_0$ is based on the depolarization of the surface emission due to the wind roughening of the sea surface. Although the three retrievals come from the same satellite sensor, their error characteristics can be considered independent because they respond very differently to errors in the radiance measurements.

## 2. Calibration of SSM/I radiances

The calibration of the SSM/I radiances has been an on-going project at RSS, and recently the 6$^{th}$ generation of SSM/I products was released (S17). The earlier versions of SSM/I retrievals were sufficiently accurate for monitoring the sea-ice extent and atmospheric water vapor because these two retrievals are relatively robust, requiring calibration accuracies at the 0.2 K level. However some of the other retrievals like wind speed are more sensitive to calibration errors. With this in mind, one of the primary objectives in the implementation of SSM/I Version 6 (V6) is to provide the community with a climate-quality wind speed dataset. In addition to a better calibration of the radiances, improved retrieval algorithms are implemented in V6. The algorithm improvements are particularly beneficial for the rain rate retrieval.

The calibration method for V6 closely follows that used for the intercalibration of the MSUs (S18). Like the MSUs, some of the SSM/Is exhibit errors that are correlated with the hot-load target temperatures, and we remove these errors using the MSU "target factor" approach (S18). The target-factor method was also used for SSM/I Version 5 (V5), but there were two problems. First, the V5 target factors for the F14 SSM/I were derived from the first 3 years of observations during which there was little variability in the hot-load temperature. Subsequently, the orbit for F14 drifted, its hot load began to experience very large swings in temperature, and the V5 target factors over-compensated for this change in temperature. For V6, we rederived the target factors using all of the F14 observations and verified that the new values worked appropriately for the entire F14 time period.

The second problem related to the F10 target factors. When the F10 observations are compared with simultaneous observations from other SSM/Is, a relatively large error becomes apparent. The error varies like a cosine function with a period of one year. In V5, we attempted to remove this error using the target factor method, which resulted in suspiciously large target factors. Subsequent analysis indicated that the correlation of the F10 error with the hot-load temperature (which also varied annually as a cosine) was coincidental. The true cause of the error is related to attitude anomalies in the F10 spacecraft. The launch of F10 was not completely successful, and the eccentricity of its orbit was large. This resulted in a relatively large variation in the Earth incidence angle over an orbit. In V6, the F10 error is modeled as an error in the reported incidence angle rather than an error related to the hot-load temperature.

A number of other refinements were implemented with V6 including using $10^{o}$ zonal intersatellite offsets rather than a single value. The V6 calibration also benefits from using a longer time period (1987-2006) as compared to V5 (1987-2001). The V6 ocean products are now freely available at www.remss.com.

## 3. Validation of the SSM/I winds and estimation of error bars

To validate the V6 SSM/I wind speeds, comparisons are made with ocean buoys and satellite scatterometer wind retrievals. The buoy measurements come from three networks of moored ocean buoys. The first two networks are the Tropical Atmosphere-Ocean (TAO/TRITON) network in the equatorial Pacific and the Pilot Research Moored Array in the Tropical Atlantic (PIRATA), both operated by NOAA's Pacific Marine Environmental Laboratory (PMEL) (S19, S20). The US National Data Buoy Center (NDBC) operates the third network, which consists of buoys in coastal regions around the continental United States, Alaska and Hawaii (S21). Care must be taken when doing the buoy validation. Due to their particular location with respect to ocean currents, upwelling area, atmospheric stability, and wind fetch, each buoy has a unique wind speed bias relative to the satellite retrieval of wind stress. This wind bias must be removed before doing the long-term stability validation or else buoys at new locations coming on-line and buoys at old locations going off-line will corrupt the analysis.

The two satellite scatterometers used in the validation are the ones that flew on the first European Remote Sensing satellite (ERS-1) (1992-1996) and on NASA's QuikScat satellite (1999-present) (S22, S23). The scatterometer wind retrievals are particularly useful in that one expects scatterometers to be less prone to calibration drifts than radiometers. The scatterometer wind retrieval is based on the ratio of received power to transmitted power, and this ratio should be insensitive to instrument drift.

The satellite wind retrievals are actually a measurement of surface stress $\tau_0$. It is convenient to express $\tau_0$ in terms of an equivalent neutral stability wind speed W at 10 m elevation (S11):

$$W = \frac{1}{C_D}\sqrt{\frac{\tau_0}{\rho}} \tag{S2}$$

where $C_D$ = 0.0013 is the drag coefficient for neutral stability and $\rho$ is the surface air density. The buoy wind measurements are also converted to a 10-m neutral stability wind using the air-sea temperature difference provided by the buoy. A ±1-hour and ±50-km collocation window is used to select those buoy observations that correspond to SSM/I overpasses.

To do the wind comparisons, monthly averages are first found and then the seasonal variability is removed, thereby producing monthly wind anomalies for SSM/I, the buoys, and the two scatterometers. The correlation between the monthly anomalies of SSM/I winds and buoys winds is 0.90, and the difference of the SSM/I trend minus the buoy trend is –0.02 m $s^{-1}$ $decade^{-1}$. An error bar is assigned to the SSM/I wind trend by assuming the monthly SSM/I minus buoy wind speed difference ΔW is entirely due to errors in the SSM/I wind retrieval. The error ΔW has a standard deviation of 0.12 m $s^{-1}$ and a lag-1 (i.e., 1 month) temporal autocorrelation $r_1$ of 0.46. This temporal correlation has the effect of reducing the effective sample size $n_{eff}$ (i.e., the degrees of freedom) and results in the estimated trend error being larger than that coming from the simple least-squares method, which assumes each observation is independent. The effective sample size is given by (S24)

$$n_{eff} = n\frac{1-r_1}{1+r_1} \tag{S3}$$

where $n$ is the number of months in the time series. This gives a trend error of ±0.05 m $s^{-1}$ $decade^{-1}$ at the 95% confidence level. Essentially the same error bar is found by doing Monte Carlo simulations of a lag-1 autocorrelation timeseries.

Fig. S1 shows timeseries of the SSM/I, buoy, and scatterometer winds. To generate these timeseries, the monthly anomalies are low-pass filtered by convolution with a Gaussian distribution having a ±4-month width at half-peak power. Although the overall trend difference between SSM/I and the buoys is very small, the SSM/I-buoy wind speed difference ΔW shows features similar to the SSM/I-scatterometer ΔW. We apply a small empirical adjustment to the SSM/I winds to bring them into agreement with the buoy winds. This adjustment is simply a table of 20 numbers that correspond to the SSM/I-buoy ΔW for each year. The magnitude of these annual adjustments is about 0.1 m/s or less, and they have no effect on the overall trend. Fig. S1 shows that bringing the SSM/I into agreement with the buoys also improve the agreement with the scatterometers. The trend difference of the adjusted SSM/I wind minus the ERS-1 scatterometer and QuikScat is +0.03 m $s^{-1}$ $decade^{-1}$ (same for both scatterometers). These adjusted winds are used in our report.

## 4. The sensitivity of evaporation to changes in surface temperature

The Clausius-Clapeyron (C-C) relationship specifies how saturation vapor pressure varies with temperature. The typically quoted C-C rate of 6.5% $K^{-1}$ corresponds to a temperature of 15°C. For warmer temperatures the C-C rate is less. For example, the C-C rate is 5.8% $K^{-1}$ for a typical surface temperature of 28°C over the tropical oceans. Since most evaporation occurs over the tropics, the effective C-C rate for evaporation tends to the tropical value. Also the air density $\rho$ term in the bulk formula for evaporation varies inversely with temperature and tends to decrease the E versus temperature derivative. To model these effects, we used Eq. S1 to compute an average evaporation over the world's oceans assuming a realistic SST field. The calculation is then repeated adding 1°C to the SST field, and the evaporation increases by 5.7%. Thus we consider 5.7% $K^{-1}$ as a typical rate for evaporation.

## 5. Using Version 6 over-ocean precipitation retrievals as compared to GPCP

To characterize the variability of rain over the ocean for the last two decades, we use our V6 SSM/I precipitation retrievals rather than the GPCP values. We have more confidence in the long-term calibration of V6 rain retrievals as opposed to the GPCP, which is a blend of retrievals from different types of satellites. As a test case, we repeated our analysis using the GPCP rain over the ocean rather than the V6 retrievals. Similar results were obtained, but the correlation between E and P was not as high. The E versus P correlation dropped from 0.68 to 0.57, and the global trend for P was 1.1% $decade^{-1}$ as compared to 1.4% $decade^{-1}$ for the standard analysis.

Although we have more confidence in the temporal variability of the V6 SSM/I rain product, the GPCP product has undergone extensive validation and probably is more accurate in an absolute sense. Accordingly, we adjusted the V6 rain rates to agree with the GPCP values in an absolute sense. This adjustment increased the V6 rain rates by 18% with most of the adjustment occurring in the middle latitudes. There is no time component to this adjustment and hence it does not affect temporal statistics given in the report.

## 6. Estimating an error bar for the precipitation and evaporation trends

When averaged globally over monthly time scales, precipitation and evaporation must balance except for a negligibly small storage term. This E=P constraint provides us with an error estimate for our derived values of E and P. The standard deviation of the monthly E-P values is 2.2%, and we assume the errors in E and in P contributed equally to E-P difference. The lag-1 (i.e., 1 month) temporal autocorrelation $r_1$ of E-P is 0.22. Following the method described above for assigning an error bar to the wind trend (S24), we find the trend error in precipitation and evaporation to be $\pm 0.5$ % at the 95% confidence level.

## 7. Response of atmospheric general circulation to global warming

The response of general atmospheric circulation to global warming is a complex process that is yet to be resolved. The weakening of the equator-to-pole temperature gradient, which is predicted by most models, suggests a weakening of winds. However, other factors are also important. The Walker Circulation responds to east-west temperature gradients (S25). If the

continents warm more than the ocean, this will affect winds. Mesoscale convection may increase in the tropics due to warmer sea surface temperatures. Small changes in the tropical lapse rate or atmospheric static stability could have a significant impact on circulation (S26). Satellite measurements of the thermal radiation emitted by the Earth suggest a strengthening of tropical general circulation during the 1985-2000 period (S27), and reanalyses indicate the Hadley cell has strengthened over the last several decades, contrary to the model predictions (S28). On the other hand, Indo-Pacific sea level pressure records from 1861 to present indicate a decrease in the Walker circulation, more in line with model predictions (S29).

## Supporting Online Material: Figure

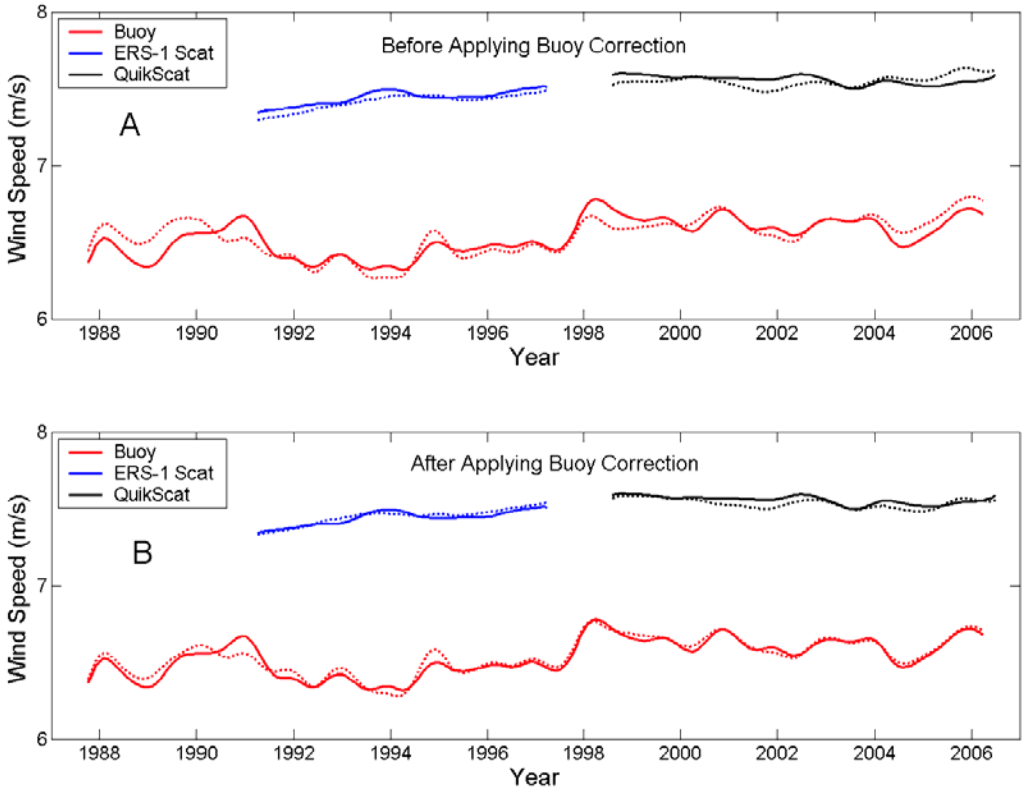


**Fig. S1**. A comparison of SSM/I wind retrievals with buoy winds and wind retrievals from satellite scatterometers. (A) The red curves show the results from collocated SSM/I and buoy observations. The solid line is the buoy wind and the dotted line is the collocated SSM/I wind. In producing the timeseries, the seasonal variability is removed and a ±4-month smoothing window is applied. Similar comparisons of the SSM/I collocated with the ERS-1 scatterometer and the QuikScat scatterometer are shown by the blue and black curves, respectively. The solid lines are the scatterometer winds and the dotted lines are the SSM/I winds. (B) Same as (A) except that a small correction has been applied to the SSM/I winds to match the buoy winds on a yearly basis. Note that this correction also improves the agreement of SSM/I with the scatterometers. The average wind speed for the buoy collocations is lower than that for the scatterometer collocations because many of the buoys are in the tropics where winds are generally lower than the global mean value of 7.5 m $s^{-1}$.

## Supporting Online Material: References and Notes


S1. W. D. Collins *et al.*, "Description of the NCAR Community Atmosphere Model (CAM 3.0)", *NCAR Technical Note*, NCAR/TN-464+STR (2004).

S2. R. W. Reynolds, N. A. Rayner, T. M. Smith, D. C. Stokes, W. Wang, *J. Climate*, **15**, 1609 (2002).

S3. N. A. Rayner *et al., J. Geophys. Res*, **108**, 10.1029/2002JD002670 (2003). We used the MOHMAT43N dataset downloaded from http://www.hadobs.org.

S4. J. R. Christy *et al*., *Geophys. Res. Lett.*, **28**, 183 (2001).

S5. C. A. Mears, F. J. Wentz, *Science*, **309**, 1548 (2005); published online 11 August 2005 (10.1126/science.1114772).

S6. J. F. B. Mitchell, C. A. Wilson, W. M. Cunnington, *Q. J. R. Meteorol. Soc*., **113**, 293 (1987).

S7. S. J. Worley, S. D. Woodruff, R. W. Reynolds, S. J. Lubker, N. Lott, *Int. J. Climatol.*, **25**, 823, 10.1002/joc.1166 (2005). The marine monthly summaries of the enhanced (ships+buoys) ICOADS 2.3 dataset downloaded from http://dss.ucar.edu/pub/coads.

S8. M. R. Allen, W. J. Ingram, *Nature*, **419**, 224 (2002).

S9. P. Peixoto, A. H. Oort, *J. Climate*, **9**, 3443 (1996).

S10. F. J. Wentz, M. Schabel, *Nature*, **403**, 414 (2000).

S11. J. P. Peixoto, A. H. Oort, *Physics of Climate*, (Springer-Verlag, New York, 1992), pp. 170-172, 228-237.

S12. R. F. Adler *et al*., *J. Hydrometeor*., **4**,1147 (2003).

S13. A. Ohmura, M. Wild, *Science*, 298, 1345 (2002).

S14. F. J. Wentz, *J. Geophys. Res*., **102**, 8703 (1997).

S15. F. J. Wentz, "User's manual SSM/I antenna temperature tapes", *RSS Technical Report 120191* (1991).

S16. D. J. Cavalieri, P. Gloersen, C. L. Parkinson, H. J. Zwally, J. C. Comiso, *Science*, **278**, 1104 (1997).

S17. SSM/I V6 products are at http://www.ssmi.com/ssmi/ssmi_description.html.

S18. C. A. Mears, M. Schabel, F. J. Wentz, *J. Climate*, **16**, 3650 (2003).

S19. M. J. McPhaden, *Bull. Am. Met. Soc*., **76**, 739 (1995).

S20. J. Servain *et al.*, *Bull. Am. Met. Soc.*, **79**, 2019 (1998).

S21. D. Gilhousen, *J. Atm. Ocean. Tech*., **4**, 94 (1987).

S22. E. Attema, *Proceedings of the IEEE*, **79**, 791 (1991).

S23. M. W. Spencer, C. Wu, D. G. Long, *IEEE Trans. Geosci. Remote Sens*., **38**, 89 (2000).

S24. B. D. Santer *et al*., *Science*, 287, 1227 (2000).

S25. M. L. Salby, *Fundamentals of Atmospheric Physics*, (Academic Press, New York, 1996), pp. 50-52.

S26. C. M. Mitas, A. Clement, *Geophys. Res. Lett.*, **33**, L01810 (2006).

S27. J. Chen, B. E. Carlson, A. D. Del Genio, *Science*, **295**, 838 (2002),

S28. C. M. Mitas, A. Clement, *Geophys. Res. Lett.*, **32**, L03809 (2005).

S29. G. A. Vecchi *et al*., *Nature*, **44**, 73 (2006).